



# <sup>57</sup>Fe-Mössbauer spectroscopy and electrochemical activities of graphitic layer encapsulated iron electrocatalysts for the oxygen reduction reaction



Lijie Zhong<sup>a</sup>, Cathrine Frandsen<sup>b,\*</sup>, Steen Mørup<sup>b</sup>, Yang Hu<sup>a</sup>, Chao Pan<sup>a</sup>,  
Lars Niläusen Cleemann<sup>a</sup>, Jens Oluf Jensen<sup>a</sup>, Qingfeng Li<sup>a,\*</sup>

<sup>a</sup> Department of Energy Conversion and Storage, Kemitovet, 207, Technical University of Denmark, DK-2800 Kgs. Lyngby, Denmark

<sup>b</sup> Department of Physics, Building 307, Technical University of Denmark, DK-2800 Kgs. Lyngby, Denmark

## ARTICLE INFO

### Keywords:

<sup>57</sup>Fe-Mössbauer spectroscopy  
Encapsulated Fe catalysts  
Oxygen reduction reaction  
Fuel cells

## ABSTRACT

Graphitic layer encapsulated iron based nanoparticles (G@FeNPs) have recently been disclosed as an interesting type of highly active electrocatalysts for the oxygen reduction reaction (ORR). However, the complex composition of the metal-containing components and their contributions in catalysis remain unclear. As a representative catalyst of the unique encapsulated structure, a series of G@FeNPs catalysts were prepared by a high-pressure pyrolytic process with uniform and essentially identical morphologies but varied compositions. The catalysts exhibited a high onset potential of 0.85 V at 0.1 mA cm<sup>-2</sup> in acidic media. By <sup>57</sup>Fe-Mössbauer spectroscopy the iron containing components were identified including α-Fe, γ-Fe, γ-Fe<sub>2</sub>O<sub>3</sub>, and Fe<sub>3</sub>C as well as a minor doublet component due to Fe<sup>3+</sup> in high spin and/or Fe<sup>2+</sup> in low spin state. The ORR activities are evaluated in terms of the mass specific kinetic current density found to be positively correlated with the Fe<sub>3</sub>C content in the range of study, indicating involvement of the encapsulated nanoparticles in the ORR catalysis. The recognition of the Fe compositions and active sites provides new insights to the confined Fe-based ORR electrocatalysts and therefore options for further development of non-precious metal materials.

## 1. Introduction

A core subject of the proton exchange membrane fuel cell (PEMFC) has been the development of alternative cathodic electrocatalysts for the oxygen reduction reaction (ORR) to replace the currently used platinum-based catalysts. The past decades have witnessed the remarkable progress on non-precious metal catalysts (NPMCs), since the pioneering work of Co phthalocyanine was introduced by Jasinski [1]. An interesting type of materials is transition metal-based NPMCs in the form of metal-nitrogen-carbon composites (M-N-C) typically synthesized by pyrolysis [2–9]. The precursors have largely been expanded from the early macrocycle molecules such as phthalocyanines and porphyrins to a wide variety of small molecules containing nitrogen, carbon and transition metals. Breakthroughs have been achieved, for example, by the polyaniline-derived Fe-N-C with improved durability due to the low H<sub>2</sub>O<sub>2</sub> yield [4], and microporous carbon supported Fe-N-C resulting from an optimized two-step pyrolysis process with high catalytic activity [2]. Exploration of active sites has suggested that the key active motifs are the Fe<sup>2+</sup> atoms coordinated with four nitrogen atoms embedded in the in-plane carbon (Fe<sup>2+</sup>N<sub>4</sub>/C) [10,11]. This type of NPMCs exhibits high ORR activity while the stability remains the

currently focused issue.

High temperature pyrolysis of iron containing precursors, in fact, involves formation of carbon around iron nanoparticles, since the amorphous carbon dissolves in the iron phase and then assembles into graphitic carbon by atomic diffusion to the surface [12]. It is therefore natural that the pyrolytic catalysts often contain some encapsulated metallic nanoparticles [13]. Several research groups have attempted to synthesize NPMCs of the encapsulated structures. Deng et al. first demonstrated that pod-like iron nanoparticles confined in carbon nanotubes (CNTs) exhibited significant ORR activity and particularly for the stability [14]. Other metal containing components such as inorganic Fe<sub>3</sub>O<sub>4</sub> [15], Fe<sub>3</sub>C [16,17] and Fe/Fe<sub>3</sub>C [18] have also been reported in the carbon-encapsulated structures. Recently, a novel approach of high-pressure pyrolysis by Hu et al. allowed for preparation of a typical catalyst of iron-containing nanoparticles in the graphitic layer encapsulated structure [19]. Characteristics of the materials include uniform iron containing nanoparticles, in a mass content range of over 10%, encapsulated in CNTs [20] or/and graphene layers [21]. The encapsulating carbon layers are likely due to the high pyrolytic pressure, curved into hollow microspheres.

For the encapsulated NPMCs, the catalytic contribution of those

\* Corresponding authors.

E-mail addresses: [frac@fysik.dtu.dk](mailto:frac@fysik.dtu.dk) (C. Frandsen), [qfli@dtu.dk](mailto:qfli@dtu.dk) (Q. Li).

encapsulated metal containing phases is currently still much debated. On one hand, the interaction of the  $\text{FeN}_x/\text{C}$  sites with encapsulated metal containing particles was emphasized [22], which is believed to boost the ORR activity. On the other hand, removal of the inorganic metal species from the Fe-N-C catalyst was found to enhance the ORR activity [23]. Very recently, a novel approach by  $\text{Cl}_2$  etching and  $\text{H}_2$ -restoring provides encouraging results for understanding the active site [24]. The authors prepared encapsulated Fe-based catalysts that contain  $\text{FeN}_x/\text{C}$  and confined Fe species. By using  $\text{Cl}_2$  etching, both  $\text{FeN}_x/\text{C}$  and confined Fe species were converted into  $\text{FeCl}_3$  and the ORR activity was lost. Further, this treated sample underwent  $\text{H}_2$  reduction. Due to N-containing species removed in  $\text{Cl}_2$  etching, the  $\text{FeCl}_3$  can only be converted into Fe species, which excludes the existence of  $\text{FeN}_x/\text{C}$ . The recovery of ORR activity after  $\text{H}_2$  reduction demonstrates the active sites of encapsulated Fe species. This encouraging result indicates the active contribution of the inner Fe phases. Further identification of the Fe phases and correlations of the iron components with the electrochemical activity should be very informative.

In our previous work, a series of graphitic layer encapsulated iron nanoparticles ( $\text{G@FeNPs}$ ) catalysts were, by varying temperature and duration of the high-pressure pyrolysis, prepared with essentially identical morphologies but different compositions [25]. The present paper is devoted to a  $^{57}\text{Fe}$ -Mössbauer spectroscopy study on various Fe components of the wrapped metal-containing phases. The identified metal components include  $\alpha\text{-Fe}$ ,  $\gamma\text{-Fe}$ ,  $\gamma\text{-Fe}_2\text{O}_3$ ,  $\text{Fe}_3\text{C}$  as well as a minor component due to (super)paramagnetic  $\text{Fe}^{3+}$  (high spin) and/or paramagnetic  $\text{Fe}^{2+}$  (low spin). In terms of the kinetic current density, the ORR activity of the materials was evaluated. The variation of the ORR activity was found to positively correlate with the content of  $\text{Fe}_3\text{C}$ . This experimental evidence relating to encapsulated  $\text{Fe}_3\text{C}$  to the ORR activity brings new insights to the current understanding of the active sites and opens avenues to further development of high performance non-precious metal catalysts.

## 2. Experimental section

### 2.1. $\text{G@FeNPs}$ preparation

The  $\text{G@FeNPs}$  catalysts were synthesized by a high-pressure pyrolysis approach. The autoclave reactor was made of modified stainless steel Swagelok® valve parts with a quartz cup (3.3 mL). A mixture of cyanamide and ferrocene in a mass ratio of 9:1 was first well mixed and transferred to the quartz cup in the autoclave in an oxygen-free glove box. The autoclave was then tightly closed and placed into the furnace, which was pre-heated to the desired temperature and held for a certain period. The pressure inside the reactor was estimated to be around 500–600 bar by assuming formation of small gaseous molecules of the precursors during the pyrolysis, which was approximately agreement with estimation by the water vapour test [25].

Two series of catalysts were synthesized with varied pyrolytic temperatures and durations. The first series of catalysts were pyrolyzed at temperatures of 600, 700 and 800 °C for 35 min and the second were prepared at a fixed temperature of 700 °C for varied durations from 15 to 240 min. The samples are named after the pyrolytic temperature (in °C) and duration (in min), for example, sample 700–75 was pyrolyzed at 700 °C for 75 min.

**Transmission electron microscopy (TEM)** was performed on Tecnai-T20-G2 at 200KV. X-Ray diffraction was performed on a Philips PW1700 diffract-meter using a  $\text{Cu K}\alpha$  ( $\lambda = 1.5405 \text{ \AA}$ ) radiation source.

**$^{57}\text{Fe}$  Mössbauer spectra** were measured at both room temperature (295 K) and low temperature (18 K) using a  $^{57}\text{Co}$  source embedded in a rhodium matrix and a constant accelerator spectrometer. The isomer shifts were given relative to that of  $\alpha\text{-Fe}$  at room temperature. The samples for Mössbauer spectroscopy were prepared by pressing ca. 100 mg of the sample powder in to pill-shapes 15 mm in diameter and

2 mm thick.

### 2.2. Electrochemical measurements

Electrochemical tests were carried out in a standard three-electrode cell, a 5.0 mm glassy carbon disk and a carbon rod were used as the working electrode and counter electrode, respectively. The reference electrode was a saturated calomel electrode (SCE). The potential was converted into a reversible hydrogen electrode (RHE) afterwards. All the electrochemical experiments were performed on a Versa STAT3 (Princeton Applied Research) and 760C Bipotentiostat (CH Instruments) in  $\text{N}_2$  or  $\text{O}_2$ -saturated  $\text{HClO}_4$  solution. The commercial Johnson Matthey 20% Pt/C was chosen as the reference catalyst. A catalyst ink was prepared by dispersing 10 mg of catalyst into a mixed solution of 514  $\mu\text{L}$  ethanol and 80  $\mu\text{L}$  of 5% Nafion. The ink was applied on the glassy carbon rotating disk electrode (RDE) or rotating ring-disk electrode (RRDE) followed by drying in air. The catalyst loading of the Pt/C catalysts for both RDE and RRDE was  $0.25 \text{ mg cm}^{-2}$  while that of the  $\text{G@FeNP}$  catalysts was  $0.65 \text{ mg cm}^{-2}$ . The kinetic current density ( $j_k$ ,  $\text{mA cm}^{-2}$ ) was derived from the RDE measurements using the Koutecky-Levich equation:

$$\frac{1}{j} = \frac{1}{j_k} + \frac{1}{j_L} \quad (1)$$

where  $j$  and  $j_L$  are the measured current and diffusion limiting current density, respectively. The mass kinetic current density is further normalized to the total catalyst mass ( $J_k$ ,  $\text{A g}^{-1}$ ), which is the same ( $0.65 \text{ mg cm}^{-2}$ ) for all samples. For the RRDE measurements, the disk electrode was scanned at a rate of  $10 \text{ mV s}^{-1}$ , and the ring potential was held constant at 1.2 V vs. RHE. The  $\text{H}_2\text{O}_2\%$  and transferred electron number per oxygen molecule ( $n$ ) were calculated by the followed equations:

$$\text{H}_2\text{O}_2\% = 200 \frac{I_r/N}{I_d + I_r/N} \quad (2)$$

$$n = 4 \frac{I_d}{I_d + I_r/N} \quad (3)$$

where  $I_d$  is the disk current and  $I_r$  the ring current, and  $N$  is the current collection efficiency of the Pt ring, which was determined to be 0.37.

## 3. Results

### 3.1. Encapsulated structure

General characterization of the two series of  $\text{G@FeNPs}$  catalysts with varied pyrolysis temperature and duration was reported previously [25]. A brief highlight is given here, which provides a basis for the present study focusing on the encapsulated iron components and active sites by  $^{57}\text{Fe}$ -Mössbauer spectroscopy.

TEM characterization reveals that pyrolysis of ferrocene and cyanamide at 600 °C involves polymerization of the cyanamide, leading to formation of melamine-rich microspheres with ferrocene dispersed evenly in the spheres (Fig. 1). The pyrolytic temperature has a significant impact on the morphology of the catalysts. At 600 °C, microspheres around 500–700 nm in diameters were formed (Fig. 1a). At 700 °C, the microspheres maintain their morphologies but become porous as the precursors start to gradually decompose. Metal or metal carbide from decomposition of ferrocene catalyze the carbon deposition, leading to formation of uniformly distributed iron-containing nanoparticles encapsulated by the carbon layers (Fig. 1c). When the temperature was further increased to 800 °C, the microspheres were found to be less regular in shape (Fig. 1h). When the temperature is fixed at 700 °C, a pyrolytic duration of 15–35 min does not seem to be sufficient to achieve complete decomposition of the precursors. After pyrolysis for longer than 35 min, the microsphere morphology of the

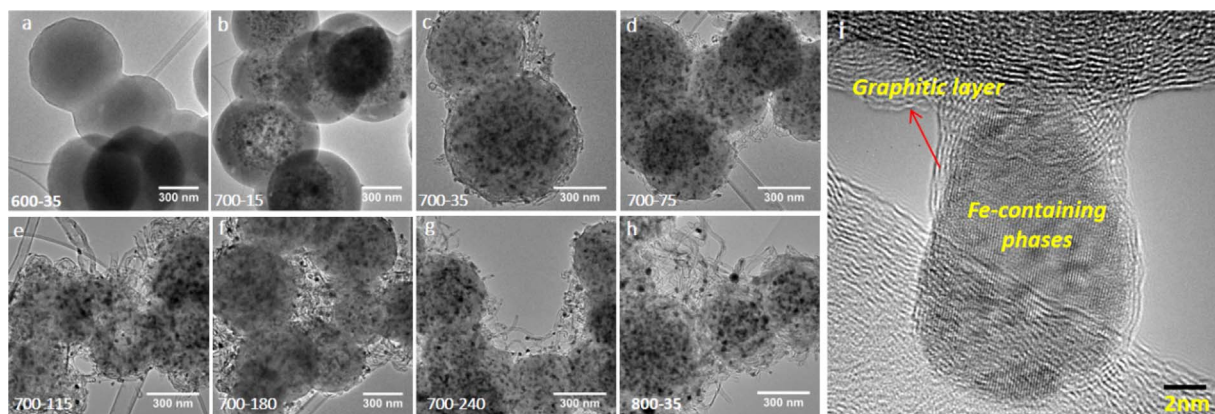


Fig. 1. (a–h) TEM images for the G@FeNPs prepared at different pyrolysis temperatures and varied durations as indicated in the figure. (i) A representative HRTEM image for G@FeNPs (700–75).

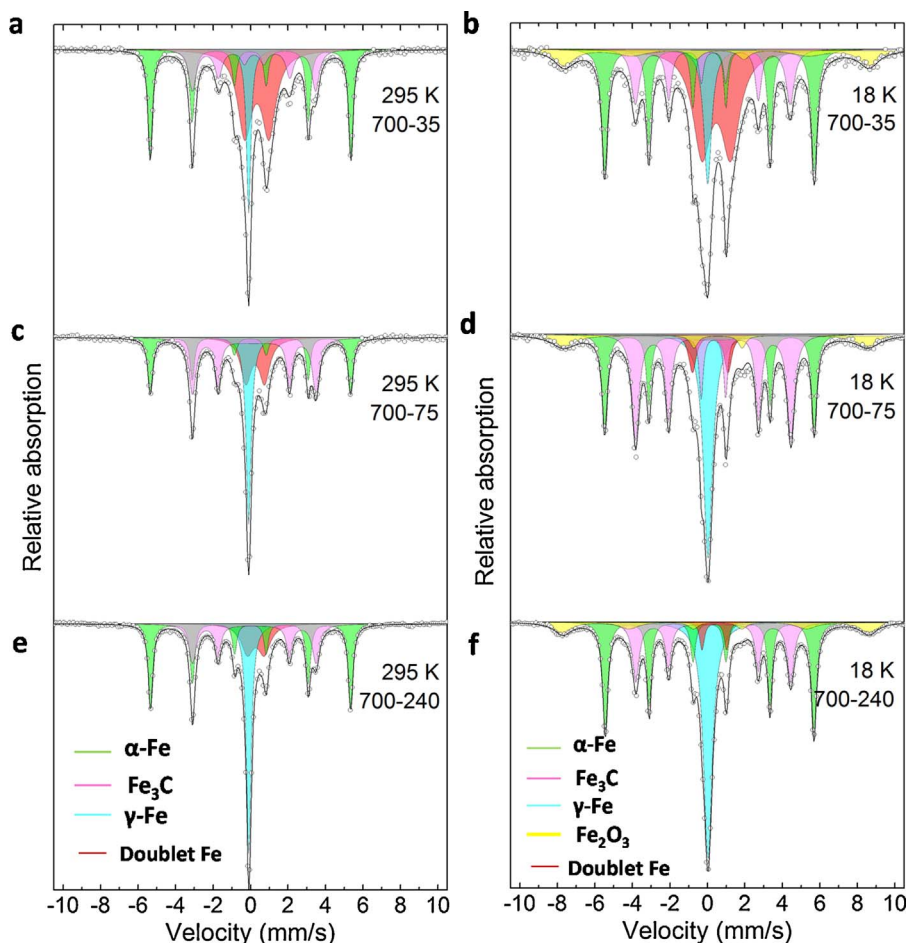


Fig. 2.  $^{57}\text{Fe}$ -Mössbauer spectra obtained at both 298 K and 18 K for selected G@FeNPs samples pyrolyzed at 700 °C for 30 min (a and b), 75 min (c and d) and 240 min (e and f).

catalysts exhibits little change though the size of the porous spheres becomes small (Fig. 1c–g). The high-resolution TEM demonstrates a well-defined encapsulated structure by a few graphitic layers (ca. 2 nm) (Fig. 1i).

Overall, using volatile small molecules of ferrocene and cyanamide as precursors, the pyrolysis temperature of 700 °C and duration of 35 mins are the cutting-off conditions for forming G@FeNPs. The high-pressure pyrolysis leads to formation of hollow micro-spheres in the size of 300–400 nm. The spheres are constituted of uniform Fe-containing nanoparticles of typically 10–20 nm, encapsulated in graphitic layers. The encapsulation structure is essential for stabilizing the nanoparticles from the chemical dissolution in acidic solutions during the acid

leaching as well as the electrochemical evaluation. As to be discussed below, significant changes in compositions of these iron-containing components are in fact observed and quantified by  $^{57}\text{Fe}$ -Mössbauer spectroscopy.

### 3.2. Recognition of Fe components by $^{57}\text{Fe}$ -Mössbauer spectroscopy

The  $^{57}\text{Fe}$ -Mössbauer spectra were recorded at both room temperature (298 K) and low temperature (18 K). Mössbauer spectra for typical samples (700–35, 700–75 and 700–240) are shown in Fig. 2. Spectra of additional samples and ferrocene precursor material are shown in Supplemental Material (Fig. S1). The spectra were fitted with three

**Table 1**

Mössbauer parameters at 295 K and 18 K for the spectra of samples 700-35, 700-75, 700-115, 700-170, 700-240 and 800-35.

Component	T K	$B_{\text{hf}}$ T	$\delta^*$ mm s <sup>-1</sup>	$\epsilon^*$ mm s <sup>-1</sup>	$\Delta^*$ mm s <sup>-1</sup>	FWHM mm s <sup>-1</sup>	Assignment
Sextet-1	295	33.1–33.2	-0.01–0.00	0.00		0.29–0.32	$\alpha$ -Fe [26, 27]
	18	34.1–34.6	0.11–0.12	0.00		0.32–0.34	
Sextet-2	295	20.4–20.6	0.18–0.19	0.01–0.02		0.45–0.65	Fe <sub>3</sub> C [10, 26]
	18	25.2–25.7	0.31–0.32	0.00		0.44–0.47	
Sextet-3	295		-			-	$\gamma$ -Fe <sub>2</sub> O <sub>3</sub> [28, 29]
	18	50.2–50.6	0.43–0.55	-0.10–0.02		1.10–1.75	
Doublet	295		0.25–0.34		0.91–1.30	0.57–0.87	Fe <sup>3+</sup> (HS) [26,30 ] and/or Fe <sup>2+</sup> (LS) [10,27,31,32]
	18		0.28–0.36		1.25–1.51	0.18–1.14	
Singlet	295		-0.09– -0.10			0.31–0.32	$\gamma$ -Fe [26]
	18		0.00–0.04			0.46–0.58	

\*  $B_{\text{hf}}$  is the magnetic hyperfine field.  $\delta$  is the isomer shift.  $\epsilon$  is the quadrupole shift in the sextets.  $\Delta$  is the quadrupole splitting of the doublets and FWHM is the width of lines 1 and 6 in the sextets and the width of the lines in the doublets and the singlet.

**Table 2**

Summary of average contents of various Fe components and ORR activities.

Sample	$\alpha$ -Fe	Fe <sub>3</sub> C	Fe <sub>2</sub> O <sub>3</sub>	Doublet Fe	$\gamma$ -Fe	$E_{1/2}$	$J_K$ (0.70 V)	H <sub>2</sub> O <sub>2</sub>	ET No.
	Mass% (of catalyst)					(V)	(A g <sup>-1</sup> )	%	
600–35	0	0	0	6.24	0.26	–	–	–	–
700–15	0.27	0.55	1.18	6.83	0.18	0.232 ± 0.026	0.24 ± 0.1	18.0	3.64
700–35	3.47	2.14	1.57	4.25	1.21	0.635 ± 0.032	2.56 ± 1.01	9.5	3.81
700–75	2.95	4.45	1.65	0.84	3.01	0.720 ± 0.006	7.84 ± 0.97	3.5	3.93
700–115	3.34	3.74	1.64	0.71	3.35	0.713 ± 0.001	7.05 ± 0.35	3.8	3.92
700–180	4.25	3.46	1.44	0.61	4.08	0.697 ± 0.009	5.44 ± 1.16	5.1	3.90
700–240	4.54	3.18	1.58	0.52	4.12	0.679 ± 0.026	5.01 ± 1.68	7.8	3.84
800–35	4.40	4.17	1.50	0.73	1.79	0.712 ± 0.002	6.96 ± 0.19	4.8	3.91

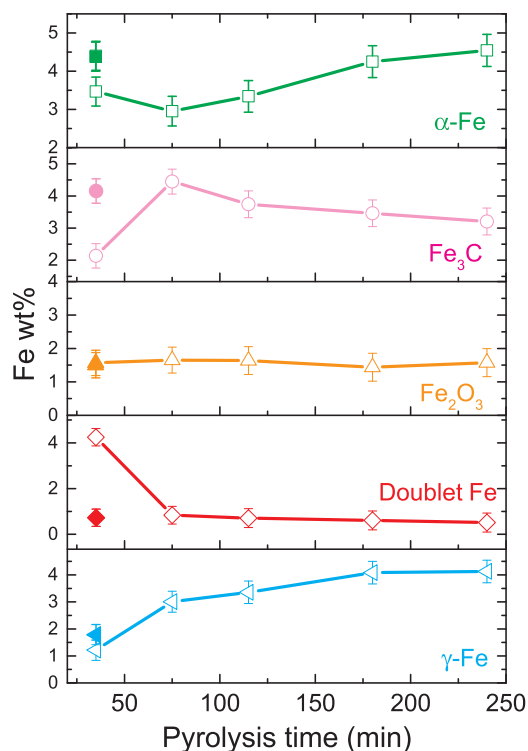


**Fig. 3.** Variation of the content of identified Fe components (%Fe) with pyrolysis time at 700 °C shown in open symbols, while solid symbols were from pyrolysis at 800 °C for 35 min. The content is based on the total mass of the catalysts as solid powders. The data were obtained from Mössbauer spectra at 18 K.

sextets, one doublet and one singlet. The parameters, estimated at 18 K and 295 K from the spectra of 700–35, 700–75, 700–115, 700–180, 700–240 and 800–35, are given in Table 1. Because of the strong overlap of the lines, it was necessary to make some constraints of the parameters. For the sextet fit, the line widths and the line intensities were constrained to be pairwise identical and the relative areas were constrained to be 3:2:1:1:2:3. In the fits of the doublets, the widths and intensities of the two lines were constrained to be identical.

The parameters of sextet 1 (green) are in accordance with those of  $\alpha$ -Fe [26,27] and the parameters of sextet 2 (magenta) are in accordance with those of Fe<sub>3</sub>C [10,26]. The isomer shift and the magnetic hyperfine field of sextet 3 (yellow, only seen in the spectra obtained at 18 K) suggest that this component can be assigned to Fe<sup>3+</sup> in the form of nanoscale  $\gamma$ -Fe<sub>2</sub>O<sub>3</sub>, which is likely originated from the atmospheric oxidation of the samples after pyrolysis, as iron nanoparticles are well known to form a passivation layer of maghemite or magnetite when exposed to air [28,29]. At 295 K, this sextet has disappeared, presumably because it has transformed to a quadrupole doublet (part of the red doublet) because of fast superparamagnetic relaxation. The singlet component (turquoise) is due to  $\gamma$ -Fe [26], which is paramagnetic at room temperature but antiferromagnetic with a very small magnetic hyperfine field at low temperature. This small hyperfine field explains the increased line width at 18 K.

The doublet component (red) has a relatively small intensity at 18 K for pyrolytic duration longer than 35 min (e.g. 700–75 and 700–240) and the lines have overlap with the sextet lines (Fig. 2c–f). Because of the low intensity and the overlap with other components, the uncertainty of the parameters for this doublet is high. The isomer shift and quadrupole splitting indicate that the doublet is due to Fe<sup>3+</sup> in the high spin (HS) state [26,30] and/or Fe<sup>2+</sup> in the low spin (LS) state [10,27,31,32]. The relative area of the doublet at 295 K is larger than at 18 K, because it has a contribution from superparamagnetic maghemite. It is likely that this doublet contains contributions from different



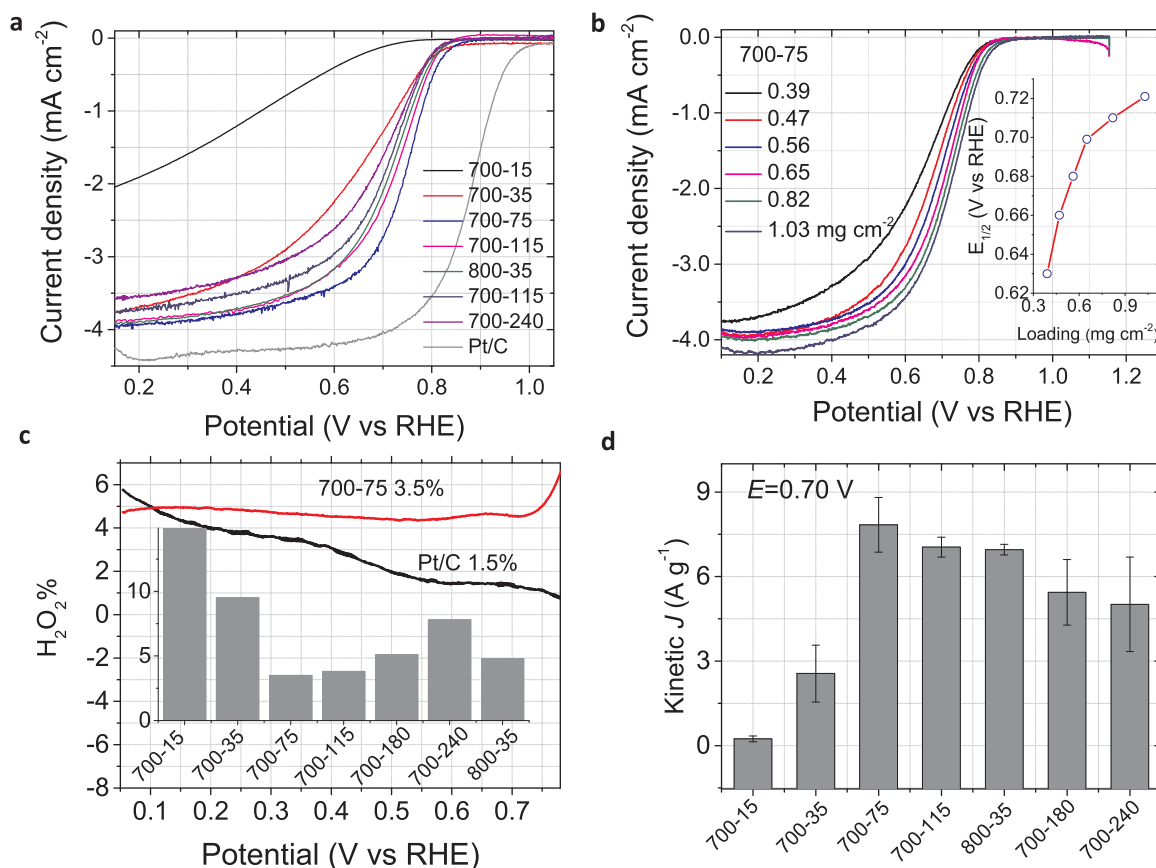


**Fig. 4.** ORR electrochemical activities of G@FeNP catalysts. (a) RDE polarization curves for G@FeNP catalysts in O<sub>2</sub>-saturated 0.1 M HClO<sub>4</sub> solution. The ORR data is replotted from reference 25. The loading of the catalyst was 0.65 mg cm<sup>-2</sup> while that of the 20% Pt/C was 0.25 mg cm<sup>-2</sup>. The rotating speed: 900 rpm. (b) RDE polarization curves for catalyst 700-75 at different mass loadings. (c) The H<sub>2</sub>O<sub>2</sub> yield for 700-75 and Pt/C determined from RRDE tests. The insert shows the comparison of the yield for all G@FeNP catalysts at 0.70 V vs. RHE. (d) Comparison of kinetic current density (J<sub>k</sub>) at 0.70 V vs. RHE for all G@FeNP catalysts. Error bars were obtained from standard deviation of 3–5 independent measurements for each catalyst.

phases. It is also noted that, for samples prepared at very low temperature (600–35) or for short pyrolysis times (15–35 min) at 700 °C, this doublet is most abundant and has a quadrupole splitting of about 1.3 mm s<sup>-1</sup> (Fig. 2a & b as well as S1, and Table 2). For samples prepared at 700 °C with longer duration (≥75 min) the doublet becomes less abundant and the quadrupole splitting is around 0.9–1.0 mm s<sup>-1</sup> (Fig. 2c–f). The possibility of an Fe<sup>2+</sup> low spin component was included in the fits, which was normally recognized as Fe<sup>2+</sup>N<sub>4</sub>/C (LS) in literature [10,27,31,32], but it turned out that the relative area was too small to obtain an unambiguous conclusion. It is apparent that this component may represent a mixture of phases containing either remaining precursors or initially formed intermediates in addition to any FeN<sub>x</sub>/C coordination sites. In the present work, no attempt was made to assign this doublet component to any specific compound(s) but we refer it to as the *doublet Fe* component in the following discussion.

### 3.3. Quantitative analysis of iron components

The relative amounts of iron in different phases were calculated from Mössbauer spectra obtained at 18 K with assumption of identical Lamb-Mössbauer factors. In parallel, the total iron content was determined by inductively coupled plasma mass spectrometry (ICP-MS) [25] based on which the amount of each phase was estimated from the Mössbauer analysis, as shown in Fig. 3. It is seen that the content of the reduced Fe form (α-Fe and γ-Fe) is steadily increasing with the pyrolytic time (at 700 °C) as well as pyrolytic temperature (the solid squares at 800 °C). The content of the *doublet Fe*, as obtained from the low temperature spectra, quickly decreases as the pyrolytic time increases from 35 to 75 min. This indicates that a major component of the mixture

phase is probably associated with the remaining precursors or the initially formed intermediates and therefore disappears when approaching the complete decomposition of the N-containing cyanamide. With a pyrolysis time of 75 min, the overall N content was about 4.1 mass% of the catalysts, and further decreased down to 2.3 mass% at 240 min. At higher pyrolytic temperature of 800 °C as low as 1.9 mass% N was detected [25]. It is of special interest that the Fe<sub>3</sub>C content was found to peak at the pyrolytic time of 75 min with fast increase before and slow decrease after this point.

### 3.4. ORR electrochemical evaluation

The ORR polarization curves obtained on the rotating disk electrode for G@FeNPs in acid media are shown in Fig. 4a. The samples pyrolyzed at below 700 °C with little formation of metallic sites showed no ORR activities while a prominent enhancement was observed for sample 700-15. For sample 700-35, the ORR activity was remarkably enhanced. The half-wave potential (E<sub>1/2</sub>) increased with the pyrolytic time from 15 to 35 min, peaked for sample 700-75 and then followed the order of 700-115 > 800-35 > 700-180 > 700-240. The 700-75 sample exhibited also the highest onset potential of 0.85 V (at 0.1 mA cm<sup>-2</sup>) (Fig. 4a), which was further increased to 0.87 V at higher catalyst loadings (1.03 mg cm<sup>-2</sup>, Fig. 4b).

The rotating-ring-disk-electrode (RRDE) measurement showed a very low H<sub>2</sub>O<sub>2</sub> yield (ca. 3.5%) and an electron transfer number (ET No.) of 3.9 for the 700-75 sample (Fig. 4c). In addition, the stability of the catalysts was found to have a small degradation by a 25 mV shift of the E<sub>1/2</sub> after 10,000 cycles from the potential between 0.6–1.0 V (vs RHE) [25]. Compared with recent literatures of similar encapsulated

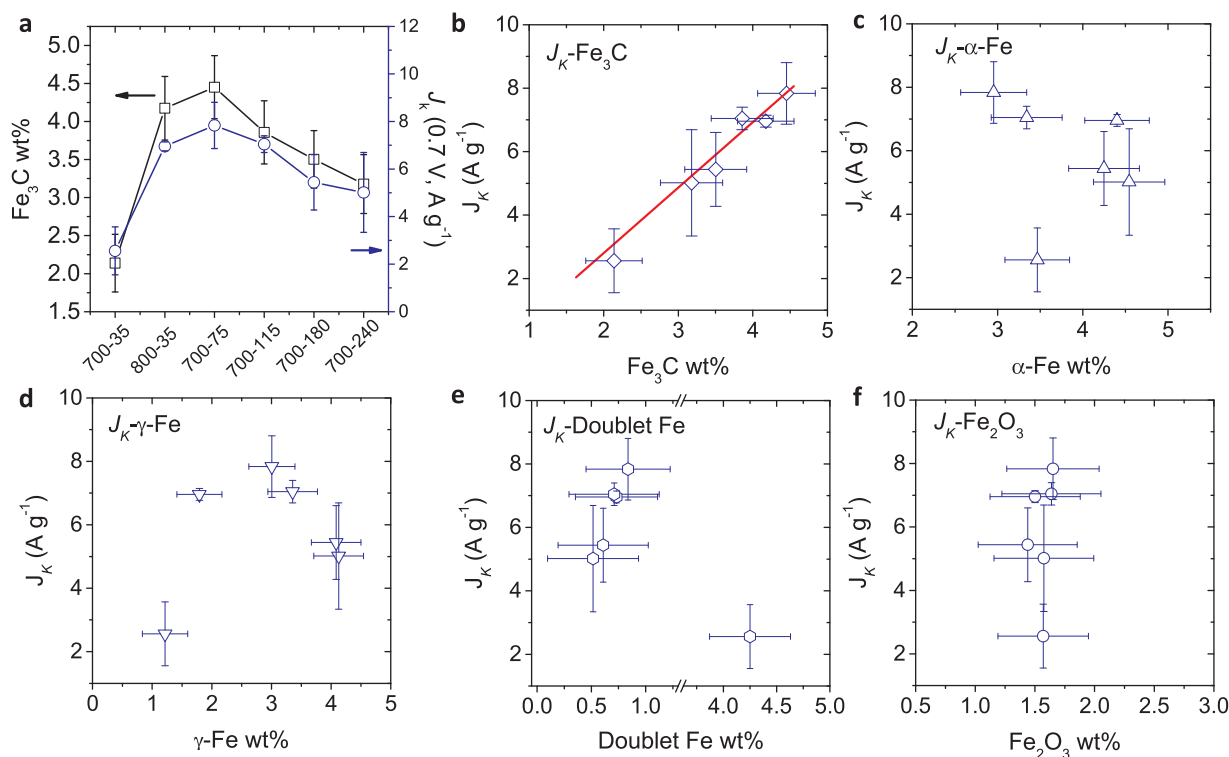


Fig. 5. Identification of ORR active sites. (a) Mass specific kinetic current density  $J_k$  at 0.70 V vs. RHE and the  $\text{Fe}_3\text{C}$  content for samples prepared by pyrolysis at 700 °C for varied durations and 800 °C for 35 min. (b–f) mass specific kinetic current density  $J_k$  at 0.70 V vs. RHE as a function of the content of various identified Fe components including  $\alpha\text{-Fe}$ ,  $\text{Fe}_3\text{C}$ ,  $\gamma\text{-Fe}$ , the doublet mixture phase and  $\text{Fe}_2\text{O}_3$ . Error bars were obtained from standard deviation of 3–5 independent RDE measurements for each catalyst.

structures [14–16,18,33], the present catalysts show relatively high activity and excellent stability in acid media. Table 2 summarizes the results for all samples discussed above. The mass kinetic current density ( $J_k$ ), obtained within the kinetically dominated potential region of around 0.7 V, is normalized to the total catalyst mass of 0.65 mg cm<sup>-2</sup> and plotted in Fig. 4d, where a peak value is observed for sample 700–75. This kinetic current density will be used for the following examination of ORR active correlations.

### 3.5. Identification of ORR active sites

Fig. 5a is a plot of the  $\text{Fe}_3\text{C}$  content and the corresponding mass specific current density  $J_k$  for the ORR of the individual catalyst sample. The plot is intended to show the correlation of the carbide content and the ORR activity. It is clearly seen that the two parameters follow the same trends and are peaking for 700–75 in the graph. The  $J_k$  is further plotted against the  $\text{Fe}_3\text{C}$  content in Fig. 5b. In the whole range of the  $\text{Fe}_3\text{C}$  content, a strong positive correlation of the electrochemical activity with the  $\text{Fe}_3\text{C}$  content was observed.

Plots similar to Fig. 5b are presented for other iron containing components in Fig. 5c–f. It should be remarked that the Fe content is the total amount of the specific iron component in the catalyst samples, expressed as mass% of the total catalyst, as obtained from the Mössbauer and ICP-MS analysis [25].

For the doublet Fe component, a positive trend was also observed except for 700–35 (Fig. 5e), though the content is not far beyond the uncertainty range of the Mössbauer analysis. It should be remarked that samples 600–35, 700–15 and 700–35 showed high doublet Fe contents but no or very poor ORR activity. It is assumed that these samples, as prepared from low temperatures and short pyrolytic times, contained an initially formed intermediate phase, which was then converted to the active  $\text{FeN}_x/\text{C}$  coordination sites during the prolonged pyrolysis. Overall, an important finding is the positive correlation of the doublet phase and  $\text{Fe}_3\text{C}$  contents with the ORR activity, suggesting that the two

metal containing components are involved in the active sites. Considering the very low content and small change of the doublet Fe phase, the notable variation of the ORR activities of these samples is assumed to be primarily correlated with the  $\text{Fe}_3\text{C}$  content. No ORR activity contribution from the other inorganic Fe-phases like  $\alpha\text{-Fe}$ ,  $\gamma\text{-Fe}$  and  $\gamma\text{-Fe}_2\text{O}_3$  can be concluded.

Because of its poor chemical stability especially in acidic electrolytes, the confined Fe species can only exist in the subsurface to the carbon layers. Previous experimental and theoretical results indicated the encapsulated Fe species exhibited activity via synergies with those surface functionalities [34]. The density function theory calculations revealed that the interaction between Fe and carbon in the CNT walls significantly enhances the activity towards the ORR [14]. Recently reported formation of Fe/ $\text{Fe}_3\text{C}$  nanoparticles in the neighbourhood of the Fe-N coordination sites was found to promote the catalytic activity [22]. In addition, the  $\text{Cl}_2$ -etching and  $\text{H}_2$ -restoring approach strongly indicates the function of encapsulated iron species [24]. However, it remains unknown that which type of encapsulated Fe is the real active component. The present results indicate that the  $\text{Fe}_3\text{C}$  among those complex Fe-containing components is the one responsible for the possible synergies through the surface carbon layer.

It is worth mentioning that the attempted pyrolysis of N-free precursors (ferrocene and durene) [25] gave poorly defined morphologies and reduced Fe components with some but limited ORR activity. Post treatment of the N-free materials under an  $\text{NH}_3$  atmosphere improved the ORR activity but remained lower than that of the present catalysts.

## 4. Conclusions

By varying temperature and duration of the high-pressure pyrolysis a series of catalysts were prepared with uniform spherical morphologies of graphitic layer encapsulated iron based nanoparticles ( $\text{G@FeNPs}$ ) but varied contents of metal containing components. The catalysts exhibited excellent catalytic activities towards ORR in acidic media. By

means of  $^{57}\text{Fe}$ -Mössbauer spectroscopy the iron containing components were identified including  $\alpha\text{-Fe}$ ,  $\gamma\text{-Fe}$ ,  $\gamma\text{-Fe}_2\text{O}_3$ ,  $\text{Fe}_3\text{C}$  as well as a paramagnetic Fe mixture phase, the content of which were estimated. Establishment of correlation of the ORR activities, in terms of the mass specific kinetic current density, with the content of various metal containing components was attempted. The  $\text{Fe}_3\text{C}$  content, within the entire studied composition range, showed a strong correlation with the ORR catalytic activity, indicating possible involvement of the nanoparticles in the ORR catalysis. Little correlation of the activity was found with other iron components present in the catalysts.

## Acknowledgements

This work has received financial support from Innovation Fond Denmark (4 M Centre 0603-00527B and Non-Precious 4106-00012B) and ForskEL program (UPCAT 2015-1-12315).

## Appendix A. Supplementary data

Supplementary data associated with this article can be found, in the online version, at <http://dx.doi.org/10.1016/j.apcatb.2017.09.014>.

## References

- [1] R. Jasinski, *Nature* 201 (1964) 1212–1213.
- [2] M. Lefevre, E. Proietti, F. Jaouen, J.-P. Dodelet, *Science* 324 (2009) 71–74.
- [3] Z. Chen, D. Higgins, A. Yu, L. Zhang, J. Zhang, *Energy Environ. Sci.* 4 (2011) 3167–3192.
- [4] G. Wu, K.L. More, C.M. Johnston, P. Zelenay, *Science* 332 (2011) 443–447.
- [5] G. Wu, P. Zelenay, *Acc. Chem. Res.* 46 (2013) 1878–1889.
- [6] W. Xia, A. Mahmood, Z. Liang, R. Zou, S. Guo, *Angew. Chem. Int. Ed.* 55 (2015) 2650–2676.
- [7] W. Gu, L. Hu, J. Li, E. Wang, *J. Mater. Chem. A* 4 (2016) 14364–14370.
- [8] J. Li, S. Ghoshal, W. Liang, M.T. Sougrati, F. Jaouen, B. Halevi, S. McKinney, G. McCool, C. Ma, X. Yuan, *Energy Environ. Sci.* 9 (2016) 2418–2432.
- [9] C.R. Raj, A. Samanta, S.H. Noh, S. Mondal, T. Okajima, T. Ohsaka, *J. Mater. Chem. A* 4 (2016) 11156–11178.
- [10] U.I. Kramm, M. Lefevre, N. Larouche, D. Schmeisser, J.-P. Dodelet, *J. Am. Chem. Soc.* 136 (2014) 978–985.
- [11] A. Zitolo, V. Goellner, V. Armel, M.-T. Sougrati, T. Mineva, L. Stievano, E. Fonda, F. Jaouen, *Nat. Mater.* 14 (2015) 937–942.
- [12] J. Wang, H. Wu, D. Gao, S. Miao, G. Wang, X. Bao, *Nano Energy* 13 (2015) 387–396.
- [13] H.T. Chung, J.H. Won, P. Zelenay, *Nat. Commun.* 4 (2013) 1922.
- [14] D. Deng, L. Yu, X. Chen, G. Wang, L. Jin, X. Pan, J. Deng, G. Sun, X. Bao, *Angew. Chem. Int. Ed.* 52 (2013) 371–375.
- [15] J. Liang, R.F. Zhou, X.M. Chen, Y.H. Tang, S.Z. Qiao, *Adv. Mater.* 26 (2014) 6074–6079.
- [16] W. Yang, X. Liu, X. Yue, J. Jia, S. Guo, *J. Am. Chem. Soc.* 137 (2015) 1436–1439.
- [17] B.Y. Guan, L. Yu, X.W. Lou, *Energy Environ. Sci.* 9 (2016) 3092–3096.
- [18] J. Wang, G. Wang, S. Miao, X. Jiang, J. Li, X. Bao, *Carbon* 75 (2014) 381–389.
- [19] Y. Hu, J.O. Jensen, W. Zhang, L.N. Cleemann, W. Xing, N.J. Bjerrum, Q. Li, *Angew. Chem. Int. Ed.* 53 (2014) 3675–3679.
- [20] Y. Hu, J.O. Jensen, W. Zhang, S. Martin, R. Chenitz, C. Pan, W. Xing, N.J. Bjerrum, Q. Li, *J. Mater. Chem. A* 3 (2015) 1752–1760.
- [21] Y. Hu, J.O. Jensen, W. Zhang, Y. Huang, L.N. Cleemann, W. Xing, N.J. Bjerrum, Q. Li, *ChemSusChem* 7 (2014) 2099–2103.
- [22] W.-J. Jiang, L. Gu, L. Li, Y. Zhang, X. Zhang, L.-J. Zhang, J.-Q. Wang, J.-S. Hu, Z. Wei, L.-J. Wan, *J. Am. Chem. Soc.* 138 (2016) 3570–3578.
- [23] U.I. Kramm, I. Herrmann-Geppert, J. Behrends, K. Lips, S. Fiechter, P. Bogdanoff, *J. Am. Chem. Soc.* 138 (2016) 635–640.
- [24] J.A. Varnell, C. Edmund, C.E. Schulz, T.T. Fister, R.T. Haasch, J. Timoshenko, A.I. Frenkel, A.A. Gewirth, *Nat. Commun.* 7 (2016) 12582.
- [25] L. Zhong, Y. Hu, J. Sværke, C. Pan, L.N. Cleemann, J.O. Jensen, Q. Li, *Int. J. Hydrogen Energy* (2017), <http://dx.doi.org/10.1016/j.ijhydene.2017.07.093>.
- [26] B. David, N. Pizurova, O. Schneeweiss, V. Kudrle, O. Jasek, P. Synek, *Jpn. J. Appl. Phys.* 50 (2011) 08JF11.
- [27] U.I. Kramm, I. Abs-Wurmbach, I. Herrmann-Geppert, J. Radnik, S. Fiechter, P. Bogdanoff, *J. Electrochem. Soc.* 158 (2011) B69–B78.
- [28] L.T. Kuhn, A. Bojesen, L. Timmermann, M.M. Nielsen, S. Mørup, *J. Phys. Condens. Matter* 14 (2002) 13551–13567.
- [29] A. Scrimshire, A.L. Lobera, R. Kultyshev, P. Ellis, S.D. Forder, P.A. Bingham, *Croat. Chem. Acta* 88 (2015) 531.
- [30] P. Güthlich, E. Bill, A.X. Trautwein, *Mössbauer Spectroscopy and Transition Metal Chemistry*, Springer Heidelberg, 2011.
- [31] U.I. Kramm, J. Herranz, N. Larouche, T.M. Arruda, M. Lefevre, F. Jaouen, P. Bogdanoff, S. Fiechter, I. Abs-Wurmbach, S. Mukerjee, J.-P. Dodelet, *Phys. Chem. Chem. Phys.* 14 (2012) 11673–11688.
- [32] U.I. Kramm, M. Lefevre, P. Bogdanoff, D. Schmeisser, J.P. Dodelet, *J. Phys. Chem. Lett.* 5 (2014) 3750–3756.
- [33] Y. Zhu, B. Zhang, X. Liu, D.-W. Wang, D.S. Su, *Angew. Chem. Int. Ed.* 53 (2014) 10673–10677.
- [34] G.Y. Zhong, H.J. Wang, H. Yu, F. Peng, *J. Power Sources* 286 (2015) 495–503.